PCCP

Accepted Manuscript

ROYAL SOCIETY OF CHEMISTRY

www.rsc.org/pccp

Physical Chemistry Chemical Physics RSCPublishing

ARTICLE

Cite this: DOI: ......

Received .....,
Accepted .....

DOI: 10.1039/........

www.rsc.org/

Organic-inorganic halide perovskite / crystalline silicon four-terminal tandem solar cells

Philipp Löper[1], Soo-Jin Moon[2], Sílvia Martín de Nicolas[1], Bjoern Niesen[1], Martin Ledinsky[1,3], Sylvain Nicolay[2], Julien Bailat[2], Jun-Ho Yum[2], Stefaan De Wolf[1], and Christophe Ballif[1,2]

Tandem solar cells constructed from a crystalline silicon (c-Si) bottom cell and a low-cost top cell offer a promising path to ensure long-term price reductions of photovoltaic modules. We present a four-terminal tandem consisting of a methyl ammonium lead triiodide ($CH_3NH_3PbI_3$) top cell and a c-Si heterojunction bottom cell. The $CH_3NH_3PbI_3$ top cell exhibits broad-band transparency owing to its design free of metallic components and yields a transmittance of >55% in the near-infrared spectral region. This allows to generate a short-circuit current density of 13.7 mA/cm^2 in the bottom cell. The four-terminal tandem yields an efficiency of 13.4 % (top cell: 6.2 %, bottom cell: 7.2 %), which is a gain of 1.8%$_{abs}$ with respect to the reference single-junction $CH_3NH_3PbI_3$ solar cell with metal back contact. We employ the four-terminal tandem for a detailed investigation of the optical losses and derive guidelines for further efficiency improvements. Based on a power loss analysis, we estimate that tandem efficiencies of ~28% are attainable with an optically optimized system based on current technology, whereas a fully optimized, ultimate device with matched current could lead up to 31.6%.

Introduction

The photovoltaics market has been dominated for decades by crystalline silicon (c-Si) solar cells, which account for a market share about 90 %[1]. Recently, efficiencies as high as 25.6% were reported for wafer-sized devices,[2] approaching the single-junction limit of ≈29 % for c-Si solar cells.[3] Additionally, the costs of photovoltaic installations scale mainly with the system area, and the key driver to reduce the price of electricity is thus the module efficiency (power per area).[4] Consequently, cell concepts enabling ultra-high efficiencies beyond the c-Si single-junction limit with low-cost fabrication are needed to ensure long-term competitiveness of photovoltaics with conventional energy sources. The most promising way towards this aim is to construct a dual-junction tandem solar cell consisting of c-Si solar cell technology combined with a high-efficiency solar cell with higher band gap. Until recently, the lack of a suitable high-efficiency top cell compatible with low-cost processing was inhibiting the fabrication of such c-Si-based tandems. However, this situation changed drastically recently with the rise of organometallic halide perovskite solar cells.[5, 6]

Since their first application as photovoltaic material,[7, 8] perovskites have demonstrated their photovoltaic potential with confirmed solar cell efficiencies up to 17.9 % to date.[9] They can be either solution-[10, 11] or vacuum-processed,[12] allowing for simple and cost-effective device fabrication, and can be deposited on glass and also on flexible materials[13, 14] and prepared at temperatures <150°C[15, 16]. Especially interesting for the application in a Si-based tandem solar cell is the reported band gap of methyl ammonium lead triiodide ($CH_3NH_3PbI_3$) between ~1.50 eV[17] and 1.57 eV.[18] $CH_3NH_3PbI_3$ is so far the perovskite material with the best efficiencies, exhibits a steep absorption edge[19] and exceptionally low sub-gap absorption.

This renders $CH_3NH_3PbI_3$ a promising candidate for the high-band gap top cell in a dual-junction tandem solar cell with a bottom cell made of a lower band-gap material such as copper indium gallium selenide (CIGS) or c-Si[20].

The tandem can either be designed as a mechanical stack of independently connected cells (four-terminal) or as a monolithic device (two-terminal). In a four-terminal tandem, the perovskite module, deposited on glass, could also serve as module glass encapsulating the bottom cell. Such a four-terminal tandem would require only marginal changes to the c-Si bottom cell, and could thus facilitate significantly the market entry for perovskite photovoltaics in the short term[21]. The monolithic tandem requires the adaptation of both cells and their interconnection with a recombination junction, representing thus a more advanced device to be realized in longer term.

While the virtues of perovskite/c-Si tandem solar cells have been pointed out by several authors,[5, 20-25] the solutions that have to be delivered to realize efficient systems have not yet been addressed in detail.

In either four- or two-terminal case, the first critical step towards a perovskite/c-Si tandem solar cell is the realization of a top cell with broad-band transparent electrodes and excellent infrared (IR) transparency.

Semi-transparent perovskite solar cells have been reported with a thin (10 nm) Au layer as back electrode,[26] reaching conversion efficiencies of 3 % to 7.5 % and showing a transmittance of 20 % at 800 nm (Ref. [26], supplementary information). In another approach, thin layers of aluminium-doped zinc oxide (AZO) and Ag were combined to a AZO/(9 nm Ag)/AZO stack electrode, leading to perovskite solar cell efficiencies of up to 7%, but the transmittance was not reported in this study.[27] For organic solar cells, semi-transparent electrodes based on silver (Ag) nanowires (NW) have been employed,[28] but require yet an additional layer for lateral transport to the Ag NW grid and ohmic contact with low resistivity.[29]

Moreover, metal-based electrodes inherently suffer from their intrinsic absorption, especially in the infrared.[30] Therefore, for high IR transparency, non-metallic electrodes have to be developed. For the application in a monolithic tandem, the electrode should moreover be applicable to wafer-sized devices (>100cm^2), compatible with industrial metallization schemes such as screen printing or copper plating.

In this article, we present an IR-transparent $CH_3NH_3PbI_3$ solar cell featuring a transparent back contact free of metallic components. We use this IR-transparent $CH_3NH_3PbI_3$ solar cell to realize a four-terminal perovskite/c-Si tandem device. Finally we perform a detailed opto-electrical analysis of the tandem system and assess the efficiency potential of optimized perovskite/c-Si tandem solar cells.

Broad-band transparent $CH_3NH_3PbI_3$ solar cell

High-efficiency perovskite solar cells are commonly prepared as a layer stack comprising a transparent conducting oxide electrode on glass, coated with either a planar[12] or a scaffold-structured[10] charge (electron or hole) transport layer, the perovskite absorber layer, the second charge transport (hole or electron) layer, and a metal rear electrode. Light enters the solar cell through the glass substrate, such that the metal rear electrode acts as a back reflector to boost photocurrent. For the four-terminal tandem presented in this article we employ the preparation route presented by Burschka et al. because of its high efficiencies of up to 15 %,[10] but replace the Au back contact by a dedicated transparent hole-collecting electrode. This cell structure, shown in Fig. 1(a), comprises fluorinated tin oxide (FTO) as TCO on glass, which is coated by a compact TiO_2 (c-TiO_2) and a mesoporous TiO_2 (m-TiO_2) layer. After a 2-step preparation of the perovskite layer, 2,2′,7,7′-tetrakis(N,N-di-p-methoxyphenylamine)-9,9′-spirobifluorene (spiro-MeOTAD) is spin-coated and serves as hole transport material (HTM).

Importantly, the transparent rear electrode is not only the first necessary development for a four-terminal tandem, but also the missing building block for the integration in a monolithic device, sketched in Fig. 1(b).

First, we prepared a transparent electrode made of 100 nm indium tin oxide (ITO) by sputter deposition directly on the spiro-MeOTAD layer. Even though the sputter process is optimized for soft deposition, the current-voltage (IV) curves, shown in Fig. 2, do not even show rectifying characteristics. Reference samples that received an evaporated Au electrode instead of the sputtered ITO on top of the spiro-MeOTAD exhibited decent cell results. From this, we conclude that the deteriorated junction characteristics in case of the ITO electrodes is likely related to damage caused by the ITO sputter deposition process, a phenomenon well-known to detrimentally affect other solar cell technologies as well, including silicon heterojunction solar cells.[31]

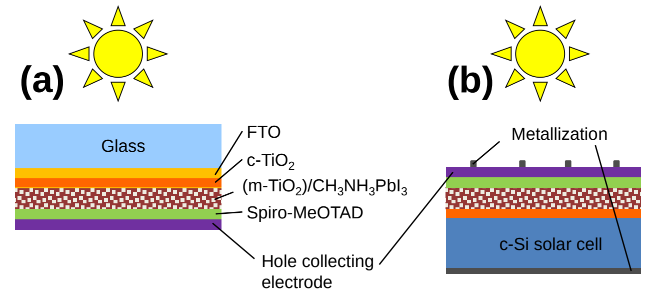

Fig. 1: (a) Schematic of the perovskite solar cell architecture based on preparing the perovskite absorber on a compact TiO_2 electrode, which is deposited on FTO-coated glass. Gold (Au) or silver (Ag) are most commonly employed as hole collecting electrode. For the four-terminal tandem, the metal hole collecting electrode has to be replaced by a broad-band transparent material. (b) Also for a monolithic perovskite/c-Si tandem, to be realized at a later stage, the transparent hole collecting electrode is a key building block as it would enable to use the established top cell preparation route also used in (a).

Recently, efficient hole-collectors for a-Si:H/c-Si heterojunction[32] and perovskite solar cells[33] were realized based on thin layers of evaporated molybdenum oxide (MoO_x). The MoO_x-based hole collectors were proven to provide a remarkably high transparency without inducing sputter damage in the active layers underneath.[32]

Inspired by these results, we tested here MoO_x layers as hole-collecting buffer layer, capped with 100 nm ITO to provide lateral conductivity to the metallization. With this design, rectifying properties were obtained both in the dark and under illumination as shown by the IV curves in Fig. 2, resulting in a

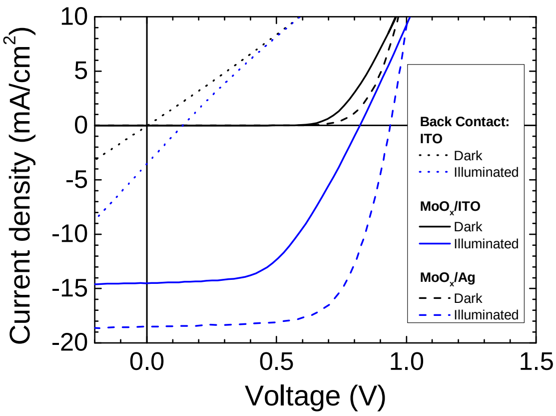

Fig 2.: Current-voltage curves in dark and under illumination of perovskite solar cells with ITO (dotted line), MoO_x/ITO (line), and MoO_x/Ag (dashed line) back contact.

conversion efficiency of 6.2 % with an active area of 0.2773 cm^2. This result was achieved with a 30 nm MoO_x buffer layer, yielding an open-circuit voltage (V_{OC}) of 821 mV, a short-circuit current density (J_{SC}) of 14.5 mA/cm^2 and a fill factor (*FF*) of 51.9 %. Fig. 2 also shows the IV curves of a reference cell, which was co-processed with the IR-transparent cell but received an evaporated Ag electrode instead of the sputtered ITO. This cell exhibits a decent performance (J_{SC}=18.51 mA/cm^2, V_{OC}=938 mV, *FF*=67 %) with an efficiency of 11.6 %.

Obviously, replacing the Ag back contact by ITO strongly affects all cell parameters. The cell with Ag back contact exhibits a higher external quantum efficiency (Fig. S1, supporting information) over the full spectral range, especially at higher wavelengths (500 nm to 800 nm), demonstrating the better light trapping due to the back reflecting properties of the Ag back contact.

The discrepancy in V_{OC} between the two cells can most likely be explained with the process-induced damage of the ITO sputter deposition -also known from a-Si:H/c-Si heterojunction solar cells[31]- being insufficiently shielded by the MoO_x layer.

To analyse the origin of the FF loss, we calculate the cells' series resistances from their dark and light IV curves according to Dicker (Eq. 3 in Ref. [34]). The cell with MoO_x/Ag back contact has a series resistance of 7.3 Ω/sq, and an associated FF loss of 11.4 %. However, the cell with transparent MoO_x/ITO back contact is affected by a series resistance of 19.6 Ω/sq, resulting in a FF loss of 24.6 $\%_{abs}$. Interestingly, the two cells differ ony marginally in their series-resistance-free FF (1.6 $\%_{abs}$), indicating that the FF is not affected by the ITO sputter process.

While the perovskite cell with transparent MoO_x/ITO back contact does not reach the performance of high-efficiency devices yet, its efficiency is comparable to that of other recently presented results with semi-transparent electrodes.[26, 27] In contrast to the latter, however, the cell presented here features transmission not only in the visible, but also in the near-infrared up to 1200 nm (discussed below), which makes this device suitable as top cell for a c-Si-based tandem.

Owing to the decent V_{OC} and *FF* values of the MoO_x/Ag reference cell, we expect that the performance of the IR-transparent cell can be boosted to the level of state-of-the-art perovskite devices by fine-tuning the ITO deposition.

Four-terminal $CH_3NH_3PbI_3$/c-Si tandem solar cell

As in a tandem the c-Si bottom cell operates with reduced generated excess carrier density with respect to standard conditions (0.1 Wcm^{-2} irradiance), it has to be adequately designed to convert the light transmitted through the top cell in an optimal way. In brief, the bottom cell should fulfil two requirements: First, it should exhibit an excellent IR response to utilize the transmitted light as well as possible. Secondly, it should feature well-passivated surfaces and contacts to enable a high open-circuit voltage even at low excess carrier densities. The class of c-Si solar cells that fulfils these two requirements best are a-Si:H/c-Si heterojunction solar cells because of their low parasitic absorption in the infrared[35] and excellent surface passivation also at low excess carrier density.[36]

Combining the top cell with transparent MoO_x/ITO electrode discussed above with an a-Si:H/c-Si heterojunction bottom cell, we realized a first perovskite/c-Si tandem solar cell, shown in Fig. 3a. We evaluated the performance of this four-terminal tandem with EQE measurements of the two subcells, i.e. the top cell and the top-cell-filtered bottom cell, and IV measurements of the two cells at the illumination conditions in the tandem configuration.

The EQE of the four-terminal tandem is shown in Fig. 3b. The top cell EQE peaks between 400 nm and 460 nm at 76 %, and then decreases monotonically towards the $CH_3NH_3PbI_3$ band gap at ~800 nm. For comparison, we also plot in Fig. 3b the absorptance *A* of a $CH_3NH_3PbI_3$ layer, calculated with the absorption coefficient reported in[19] in the single pass limit ($A=1-\exp(-\alpha\cdot d)$) for a typical absorber thickness of d=200 nm. The EQE decreases towards the band gap and its similarity to the single pass limit suggests that the degree of light trapping in the top cell is low. Photons between 500 nm and 800 nm that are not converted in the top cell contribute at least partially to bottom cell current. The total tandem EQE is approximately constant up to the $CH_3NH_3PbI_3$ band gap. For photon energies below the $CH_3NH_3PbI_3$ band gap (>800 nm), up to 58% of the photons that are incident on the tandem system are transmitted through the top cell and utilized by the c-Si bottom cell.

The bottom cell J_{SC} calculated from the EQE measurement is 13.7 mA/cm^2. With this current, the bottom cell exhibits an open-circuit voltage of 689 mV and a fill factor of 76.7 %. The IV curves of both subcells of the tandem are shown in Fig. 3c. In a final tandem module, the two (top and bottom) submodules will have different maximum power points, which makes an

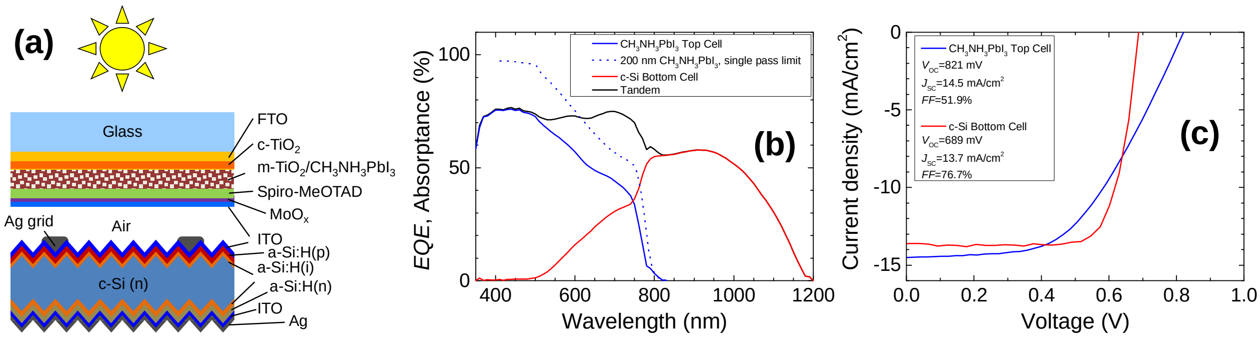

Fig. 3: a) Schematic of the mechanically stacked four-terminal tandem. The system consists of a high-efficiency a-Si:H/c-Si heterojunction solar cell and a high-efficiency $CH_3NH_3PbI_3$ top cell with a metal-free MoO_x/ITO transparent electrode. b) External quantum efficiency and c) current-voltage curves of the two individually connected subcells in the four-terminal perovskite/Si tandem solar cell.

individual connection of each submodule to a separate inverter necessary. The total four-terminal tandem efficiency is thus the sum of the individual subcell efficiencies. The efficiency sum of the four-terminal tandem presented here is 13.4 %, which is 1.8 $\%_{abs}$ higher than the efficiency of the reference perovskite solar cell with MoO_x/Au back contact mentioned above. Table 1 summarizes the parameters of the four-terminal tandem system.

The total EQE of the tandem system is above 70% for λ<750 nm, but strongly drops for longer wavelengths as the top cell does not contribute to photocurrent any more. We remark that without top cell, the bottom cell features an EQE >90% from 400 nm to 1000 nm, virtually utilizing all photons in this spectral region. The low tandem EQE in the infrared, but also in the visible, therefore hints at parasitic light filtering by the perovskite top cell.

We remark that an efficiency gain of 1.8 $\%_{abs}$ relative to a single-junction perovskite cell cannot justify the cost of adding a c-Si bottom cell. From the perspective of c-Si photovoltaics, the top cell is far from being sufficiently efficient and transparent to boost the efficiency of state-of-the-art c-Si cells. However, it has to be taken into account that the top cell efficiency is severely affected by at least two significant drawbacks: Firstly, the J_{SC}, V_{OC} and *FF* losses induced by the MoO_x/ITO transparent electrode, and secondly the parasitic absorption in the top cell. As the IV characteristics prove that the junction is well formed and rectifying, we expect that further process and material optimization will likely increase the top cell V_{OC} and *FF* towards state-of-the-art performance.

In the meantime, the four-terminal tandem presented here constitutes a valuable test platform for an experimental power loss analysis and enables us to assess the tandem efficiency potential.

The preliminary results presented in this article thus not only point out the complexity of realizing efficient perovskite/c-Si tandem devices, but also which solutions have to be found to compete with and even surpass high-efficiency c-Si solar cells.

Table 1: Cell parameters of the transparent and the reference perovskite solar cells, the SHJ bottom solar cell, and the resulting tandem efficiency (sum).

Cell	Hole Contact	J_{SC} (mA/cm^2)	V_{OC} (mV)	*FF* (%)	Efficiency (%)
Perovskite Reference	MoO_x/Ag	18.5	938	67.0	11.6
Perovskite Top	MoO_x/ITO	14.5	821	51.9	6.2
SHJ Bottom		13.7	689	76.7	7.2
Perovskite/SHJ Tandem					13.4

IV Current loss analysis

In the following, we present a detailed opto-electrical analysis to quantify current and power losses and assess the efficiency potential of optimized systems.

Fig. 4 depicts the transmittance (T_{Top}) spectra of the perovskite top solar cell as well as its $1\text{-}R_{Top}$ curve and absorptance ($A_{Top}=1\text{-}R_{Top}\text{-}T_{Top}$) spectrum. We also replot in Fig. 4 the EQEs shown in Fig. 3b for comparison. The EQE and absorptance of the top cell exhibit a similar spectral shape in the visible, but are offset by about 15$\%_{abs}$. The difference between absorptance and EQE can be attributed to parasitic absorption losses, i.e. absorption processes not contributing to the top cell photocurrent.

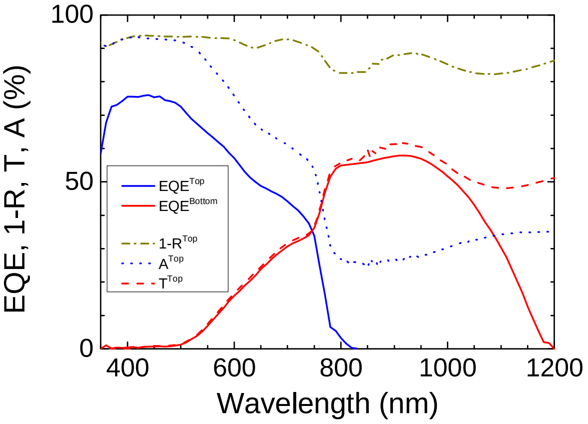

Fig. 4: Transmittance, 1-reflectance and absorptance spectra of the top cell and external quantum efficiency spectra of the top and bottom cells.

Excellent agreement can be seen between the top cell transmittance and the EQE of the bottom cell up to 1000 nm, indicating that the bottom cell is efficiently converting the incident photons to photocurrent. For wavelengths >1000 nm, the two curves begin to deviate as the bottom cell EQE decreases near the c-Si band gap. Ideally, the top cell should transmit 100% of the incident photons below the $CH_3NH_3PbI_3$ band gap. However, the data shown in Fig. 4 demonstrate that the realized top cell transmits ~55% of the light between 800 nm and 1200 nm, and absorbs between 25% and 35% of the incident photons despite the excellent sub-bad gap transparency of $CH_3NH_3PbI_3$ itself[19].

Fig. 4 thus clearly demonstrates that the tandem performance is limited by parasitic absorption in the top cell in the visible but even more in the infrared spectral region. As $CH_3NH_3PbI_3$ itself does not lead to undesired sub-band gap absorption,[19] the encountered top cell absorption losses rather have to be related to the specific top cell architecture. To elucidate the origin of the parasitic absorption, we plot the absorptance of incrementally built-up layer in Fig. 5. The layer stacks were prepared identically to the perovskite cells and resemble the structure, morphology and layer thicknesses of the perovskite cells. The FTO front electrode alone is highly transparent in the

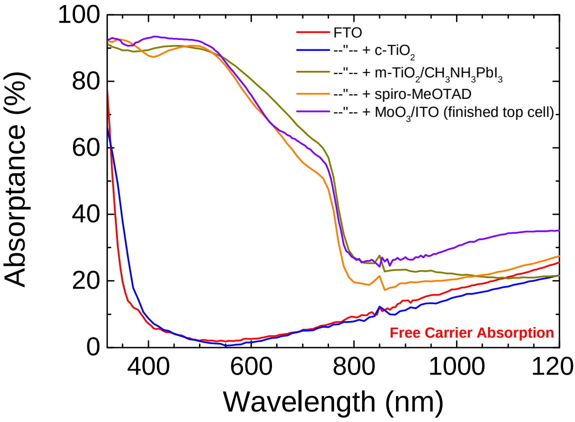

Fig. 5: Absorptance spectra of incremental layer stacks.

visible spectral range, but does exhibit pronounced absorption in the infrared. Adding the compact TiO_2 layer leaves the absorptance almost unchanged. With the mesoscopic TiO_2/perovskite compound layer, the absorptance is already close to that of the finished cell in the visible, and slightly increases in the infrared. The spiro-MeOTAD layer and the MoO_x/ITO electrode do (in this device configuration) not influence the visible absorption considerably, but both induce increased infrared absorption. In summary, Fig. 5 shows that absorption losses in the infrared are caused by the top cell components FTO, spiro-MeOTAD and ITO. These layers are highly doped, and the absorption can be attributed to free carrier absorption (FCA), which is proportional to the charge carrier density and the square of the wavelength.[37] In spiro-MeOTAD, the high doping is needed for efficient hole extraction.[38, 39] On the other hand, FTO and ITO have to provide lateral conductivity over several millimetres, and a reduced charge carrier density would compromise the fill factor. Consequently, the four-terminal tandem architecture faces a trade-off between TCO electrical properties (top cell fill factor), and minimized FCA (bottom cell current).

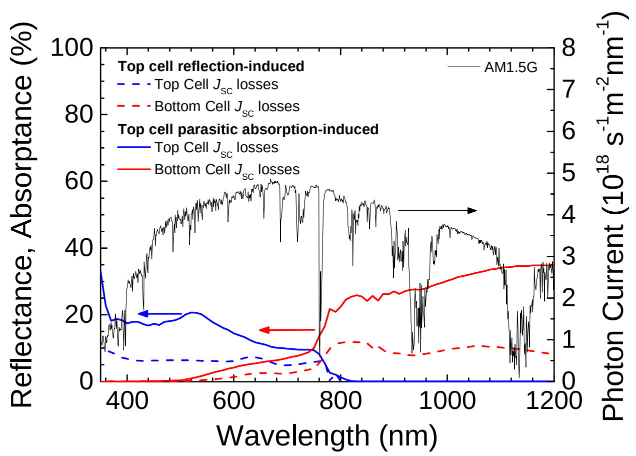

Fig. 6: Current loss spectra separated into top cell and bottom cell current losses.

To quantify the associated power losses, we separate the spectrally resolved current losses in the top cell from those in the bottom cell according to the procedure outlined in the appendix. Fig. 6 illustrates the current loss spectra of each subcell according to the loss mechanism (reflection from or parasitic absorption in the top cell). Reflection by the top cell causes current losses of 1.64 mA/cm^2 in the top, and 2.05 mA/cm^2 in the bottom cell. The most dominant current loss is caused by parasitic absorption, which accounts for 3.81 mA/cm^2 in the top, and 6.67 mA/cm^2 in the bottom cell. In total, the current losses translate to efficiency losses of 2.4 $\%_{abs}$ in the top, and 4.2 $\%_{abs}$ in the bottom cell.

V Efficiency Potential

In this section, we consider different model perovskite/c-Si tandem systems, moving from the realized perovskite/c-Si tandem presented in this article towards more optimized systems. We start with the four-terminal tandem shown in Fig. 3, denominated Case 1 in Tab. 2. Assuming that the V_{OC}- and FF-related losses caused by the transparent MoO_x/ITO electrode can be overcome by process and architecture optimization, we recalculate the efficiency with state-of-the-art junction parameters (V_{OC} and FF) taken from Ref. 10. To account for the V_{OC} illumination-dependence we recalculate V_{OC} with the one-diode model[40] (see appendix) using an ideality factor of 1. This yields a tandem efficiency of 17.6% (Case 2). As the next step to an ultimate, but still realistic limit of the tandem efficiency we use record values for the bottom cell V_{OC} and FF. Si solar cells are already close to their "technical" limit, and published world-record devices are therefore good approximates of a realistic ultimate bottom cell. The world-record c-Si solar cell is a back-contacted solar cell featuring a-Si:H/c-Si heterojunction contacts[2]. For tandem applications, however, the IR response rather than J_{SC} under full spectrum illumination is decisive. As the best reported IR performance was realized with a both-sides contacted SHJ device by

Table 2: Photovoltaic conversion efficiencies of perovskite/c-Si tandem solar cells. Case 1 summarized the demonstrator device discussed in section III. Case 2 and 3 are theoretical efficiencies calculated with published record *Voc* and *FF* values. For case 4, the current losses, calculated from the device of case 1, were added to the respective cells. Case 5 corresponds to the ideal current matched tandem discussed in section I. Values that change with respect to the preceeding case are marked red. "Experiment" denotes experimental results presented in this paper.

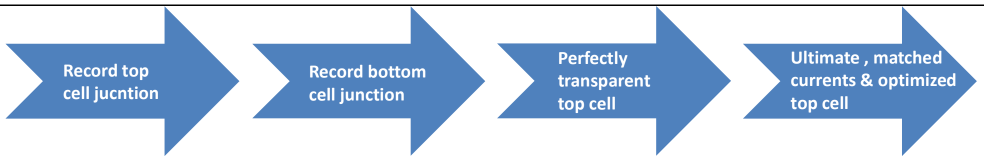

		Case 1		Case 2		Case 3		Case 4		Case 5	
Top	J_{SC}	Experiment	14.5	Experiment	14.5	Experiment	14.5	**Exp. + $J_{Loss,Top}$**	**20**	**J_{SC} matched**	**21.73**
	V_{OC}		821	**Record top**	**984.7**	Record top	984.7	Record top	992.9	**Performance goal**	**1050**
	FF		51.9		**73**		73		73		**80**
	η		6.2		10.4		10.4		14.5		18.25
Bottom	J_{SC}	Experiment	13.7	Experiment	13.7	Experiment	13.7	**Exp. + $J_{Loss,Bottom}$**	**21.4**	**J_{SC} matched**	**21.73**
	V_{OC}		689.2		689.2	**Record bottom**	**730.9**	Record bottom	739.0	Record bottom	739.3
	FF		76.7		76.7		**83.2**		83.2		83.2
	η		7.2		7.2		8.3		13.1		13.37
Tandem	η		13.4		17.6		18.7		27.6		31.62

carefully designing the rear contact,[35] we use the record values for both-sides contacted SHJ cells, V_{OC}=750 mV, J_{SC}=39.5 mA/cm^2, and FF=83.2 % for an illumination of 0.1 W/cm^2, as the ultimate bottom cell.[41] We account for the V_{OC} illumination dependence using the one-diode model[40] and an ideality factor of 0.7,[3] and obtain a tandem efficiency of 18.7 % (Case 3).

Even though this tandem cell is composed of record V_{OC} and FF values for both subcells its efficiency still falls short behind single-junction c-Si solar cells. This illustrates how severely the current losses due to reflection and parasitic absorption affect the tandem efficiency. Assuming that these optical losses can be overcome by appropriate optical design, including anti-reflective coatings and intermediate light reflectors/couplers between the perovskite and the c-Si cell, we add the J_{SC} losses determined in Section IV to the respective cells and recalculate their efficiencies. Such an optimized system, free of any parasitic absorption attains an efficiency of 27.6 % (Case 4). The efficiency improvement relative to Case 3 results from a J_{SC} gain of 5.45 mA/cm^2 in the top cell and 7.73 mA/cm^2 in the bottom cell, corresponding to efficiency gains of 4.04 % and 4.85 %, respectively. Interestingly, the tandem of Case 4 is very close to current matching conditions. As stated above, we consider a perovskite top cell with V_{OC}=1050 mV and FF=80 % to be a realistic performance goal. In a current matched tandem, represented by Case 5, an efficiency of 31.62% would be attainable with this top cell. Even with current losses of 0.5 mA/cm^2 of each of the subcells, the tandem efficiency would still be >30%.

VI Large-area four-terminal modules

The most straightforward way to realize perovskite/c-Si tandem modules is to mechanically stack a large-area perovskite module with -and couple it optically to- c-Si solar cells. In this device architecture, both subcells can be fabricated independently, yielding thus great engineering flexibility for optimization. Interconnection would be done by laser patterning the top cell to a perovskite top module as sketched in Fig. A1 (see appendix), and then wiring top and bottom modules. Alternatively to laser patterning, the top cell could also be contacted with a metal grid, but this solution is likely to be too costly. In any case, however, lateral conductance through the top cell TCOs over one cell stripe width w is needed, and can cause resistive power losses depending on the TCO sheet resistance. As free carriers in the TCOs also cause absorption and thus current losses in the bottom cell, the total tandem efficiency is a delicate balance between minimized resistive losses in the top module and minimized current losses of the bottom cell due to parasitic absorption in the top cell (see appendix for details). The trade-off between absorption and sheet resistance of a TCO can be described by the figure of merit $\langle FOM\rangle$, defined here as the inverse of the product of the effective top cell sheet resistance R_{Sh} and its weighted sub-band gap absorptance $\langle A\rangle$ (see appendix):

$$\langle FOM\rangle = \frac{1}{R_{Sh}\cdot\langle A\rangle}. \tag{1}$$

We evaluate the tandem efficiency according to the analytical model developed in the appendix (Eq. 16) for a photo-inactive interconnection width of 100 µm, which is a typical value for state-of-the-art processing, assuming an average transparency of the interconnection area m of 50%. We plot the four-terminal tandem module efficiency with the cell parameters of Case 5 (Table 2), optimized with respect to the cell stripe width, as a function of the top cell TCO sheet resistance and figure of merit in Fig. 7 (color contours). To illustrate the effect of the TCO optical properties more explicitly, we also plot in Fig. 7 the weighted top cell sub-band gap absorptance $\langle A\rangle$ (black dashed equiabsorptance lines) according to Eq. (1).

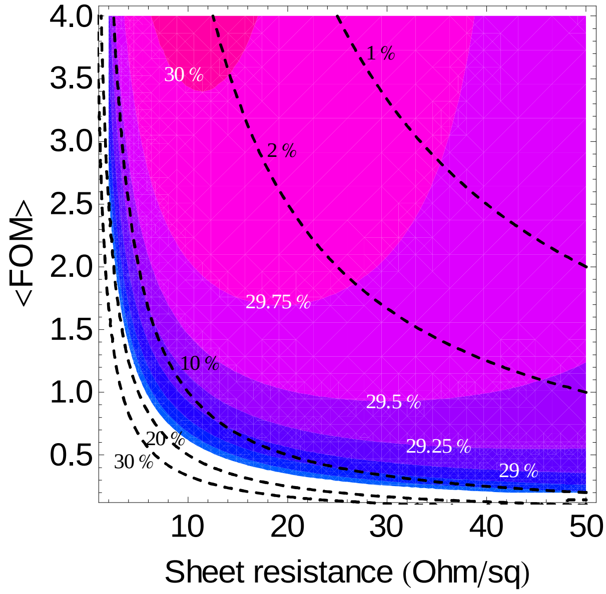

Fig. 7: Four-terminal tandem modules efficiency (color contours with white labels) and weighted top cell sub-band gap absorptance (black dashed lines with black labels) calculated with the cell parameters of Case 5 (Table 2) as a function of the sheet resistance and the weighted figure of merit of the top cell TCOs. The module efficiency was calculated for an interconnection stripe width and transparency of 100 µm and 50%, respectively, and optimized with respect to the cell stripe width. A maximum module efficiency >30% is atttained at sheet resistances of 8-13 Ω/sq with a FOM>3.5 sq/Ω.

For $\langle FOM\rangle$<1 sq/Ω, the top cell is increasingly transparent for higher sheet resistances and the tandem efficiency increases. For higher FOM (>1.5 sq/Ω), the tandem efficiency first increases for increasing sheet resistance (0<R_{Sh}<15 Ω/sq) as the TCO becomes increasingly transparent, and then decreases due to the resistive losses in the top cell. An efficiency >30 % can be reached with a TCO which yields a $\langle FOM\rangle$≥3.5 sq/Ω for a sheet resistance range of 8-13 Ω/sq.

The transparent top cell presented above yields an effective figure of merit of 0.07, calculated from the sub-band gap absorptance shown in Fig. 4 and its average sheet resistance of 52.5 Ω/sq (average of the employed FTO and ITO layers with 15 Ω/sq and 90 Ω/sq respectively). We remark that this value is an effective value, which includes absorption of the entire top cell and is moreover affected by absorption enhancement due to scattering and multiple reflections.

Finally, we evaluate the properties of TCOs optimized for solar cell applications. With ITO layers optimized for infrared transmittance,[42] a $\langle FOM\rangle$ of 0.97 can be attained when neglecting absorption in any other layers. Even higher transparency can be achieved with hydrogen-doped tin oxide (IO:H)[42] or plasma-treated zinc oxide (ZnO)[43]. These materials provide weighted figure of merits of 2.41 and 2.97, respectively, and according to Fig. 7 would thus enable tandem module efficiencies of 30 % for a wide range of TCO parameters.

Outlook

The results presented here illustrate that perovskite/c-Si tandem solar cells have the potential to surpass the c-Si efficiency record (25.6 %),[2] but they also point out the challenges that are associated with their realization.

In detail, the following development steps have to be accomplished to achieve tandem efficiencies of 30%:

a) Marginal sub-band gap absorption of the perovskite absorber material,
b) Top cell efficiency improved to the level of >18 % for wafer-sized devices,
c) Transparent top cell electrodes that do not compromise V_{OC} and FF (values in the range of 1000 mV and 80%, respectively),
d) Broad-band (500 nm-1200 nm) transparent top cell resulting in a total parasitic absorption losses of <1 mAcm^{-2}, and, for four-terminal tandems, yield a weighted figure of merit of >2.

For the $CH_3NH_3PbI_3$ material, criterion a) is fulfilled.[19] Criterion b) is met when considering recent record values on small devices,[9, 44] but module efficiencies do not exceed ~5 % so far.[45]

The transition from a top cell with >18 % efficiency (b) to a 18 % top cell with transparent electrodes (c) can likely be achieved by process and material optimization. Broad band transparency (c), however, is limited by the device architecture, as our results indicate that the standard architecture employed here induces parasitic absorption losses of 5.4 mA/cm^2 and 7.7 mA/cm^2, respectively, in the top and the bottom cell.

As the four-terminal device requires lateral conductivity, and thus sufficient doping and thickness of the two intermediate TCOs (cf. Fig. 8), it is inherently affected by parasitic absorption. Moreover, upscaling requires micro patterning of the top cell and interconnection to mini modules, further increasing optical losses. These losses can be mitigated by monolithically interconnecting the two cells, relaxing the requirements to lateral conductance and potentially eliminating completely the two intermediate TCOs (cf. Fig. 1b).

Importantly, the monolithic device also facilitates upscaling because it requires lateral conductivity only in the topmost electrode. Our results also illustrate the importance of implementing highly transparent alternatives for the doped layers (FTO, ITO and spiro-MeOTAD), such as tetrathiafulvalene derivative,[46] IO:H[42] or ZnO films.[43] The most promising candidates for the bottom cell appear to be Si heterojunction devices. Besides their excellent open-circuit voltages they feature a record-high infrared response[35]. Moreover, as a bottom cell they are not affected by optical losses in the blue, their most important drawback at full-spectrum illumination, and can thus easily be optimized for the spectrum and illumination intensity in a tandem. In addition, Si heterojunction solar cells already feature a built-in recombination junction[47] (between doped amorphous Si and TCO) which is required for a monolithic interconnection of bottom and top cells.

Finally, we remark that for optimum spectrum utilization, a material with slightly higher top cell band gap (1.7 eV...1.8 eV) and thus also higher V_{OC} would be beneficial. This underlines the importance of alternative absorber materials such as mixed iodide-bromide perovskites.[48, 49] With this material system, Noh et al. were able to achieve a band gap of 1.7 eV for a composition of $CH_3NH_3Pb(I_{0.75}Br_{0.25})_3$, a promising result in view of tandem applications.[48]

Conclusion

In this article, we presented a four-terminal perovskite/c-Si tandem solar cell and derived limiting efficiencies of practical perovskite/c-Si tandems.

The realized four-terminal tandem is based on a c-Si heterojunction bottom cell and a $CH_3NH_3PbI_3$ top cell featuring a transparent MoO_x/ITO hole contact. With the transparent MoO_x/ITO hole contact, the top cell features an impressive infrared-transparency of up to >55%. The four-terminal tandem yields an efficiency of 13.4%, with similar contributions of the top (6.2%) and the bottom cell (7.2%). We employ the four-terminal tandem as test device for an experimental power losses analysis, splitting the current losses into reflection- and parasitic absorption-induced losses based on an optical analysis, and separating them according to the respective subcell. Assuming published record values for the individual subcells, an efficiency of 27.6% would be attainable with an optimized system. Anticipating improved values for the top cell voltage (1050 mV) and fill factor (80%), we identify a tandem efficiency >30% as mid-term goal.

Acknowledgement

The project comprising this work is evaluated by the Swiss National Science Foundation and funded by Nano-Tera.ch with Swiss Confederation financing and by the Office Féedéeral de l'Energie, Switzerland, under Grant SI/501072-01.

Appendix

Spectral analysis of current losses

In order to quantify the power losses in the tandem solar cell, we split the photon current losses to those photons that would have contributed to top cell current and those that would have contributed to bottom cell current if they were not lost by reflection or parasitic absorption.

Photons that are incident on the tandem system can either be reflected by the top cell, or transmitted through it, or generate a photocurrent, or be absorbed without generating photocurrent. We denote the probabilities of the respective processes as R_{Top}, T_{Top}, EQE_{Top} and PA_{Top}, with the parasitic absorption PA_{Top} defined as the difference between absorbed photons and photons that are absorbed and collected as photocurrent, $PA_{\mathrm{Top}} = A_{\mathrm{Top}} - EQE_{\mathrm{Top}}$. The four processes fulfill the identity

$$1 = R_{\mathrm{Top}} + T_{\mathrm{Top}} + EQE_{\mathrm{Top}} + PA_{\mathrm{Top}}. \tag{2}$$

For photons that are not reflected, we can calculate the probabilities of the other three processes, T'_{Top}, EQE'_{Top} and PA'_{Top}, by normalizing with $1 - R_{\mathrm{Top}}$ (rearranging Eq. 1): $T'_{Top} = T_{\mathrm{Top}}/(1 - R_{\mathrm{Top}})$, $EQE'_{Top} = EQE_{\mathrm{Top}}/(1 - R_{\mathrm{Top}})$, and $PA'_{Top} = PA_{\mathrm{Top}}/(1 - R_{\mathrm{Top}})$. In analogy to Eq. 1, the identity

$$1 = T'_{Top} + EQE'_{Top} + PA'_{Top} \tag{3}$$

holds for these three expressions. The reflected photon flux,

$$J_R = \int R_{Top}\phi_{AM1.5G}\,d\lambda, \tag{4}$$

can thus be split up according to

$$J_R = \int R_{Top}\left(EQE'_{Top} + PA'_{Top} + T'_{Top}\right)\phi_{AM1.5G}\,d\lambda. \quad (5)$$

$\phi_{AM1.5G}$ denotes the AM1.5G solar spectrum[50] and λ the wavelength. For those photons that are neither reflected nor parasitically absorbed, we calculate the probabilities for transmission and photocurrent generation by normalization with one minus the internal fraction of not parasitically absorbed photons, $1 - PA'_{Top}$ (rearranging Eq. 2): $T''_{Top} = T'_{Top}/(1 - PA'_{Top})$, and $EQE''_{Top} = EQE'_{Top}/(1 - PA'_{Top})$, for which the identity $1 = T''_{Top} + EQE''_{Top}$ holds. We can then split up the current loss caused by parasitic absorption in the top cell,

$$J_{\mathrm{PA}'} = \int PA'_{\mathrm{Top}}\phi_{\mathrm{AM1.5G}}\,d\lambda, \quad (6)$$

into the parts affecting top and bottom cell,

$$J_{\mathrm{PA}'} = \int PA'_{\mathrm{Top}}\left(EQE''_{Top} + T''_{\mathrm{Top}}\right)\phi_{\mathrm{AM1.5G}}\,d\lambda \quad (7)$$

Using Eqs. 4 and 6 we can now separate the losses affecting top cell short-circuit current density,

$$J_{\mathrm{Loss,Top}} = \int \left(R_{\mathrm{Top}}EQE'_{\mathrm{Top}} + PA'_{\mathrm{Top}}EQE''_{\mathrm{Top}}\right)\phi_{\mathrm{AM1.5G}}\,d\lambda, \quad (8)$$

from those that affect the short-circuit current density of the bottom cell,

$$J_{\mathrm{Loss,Btm}} = \int \left(R\,T'_{\mathrm{Top}} + PA_{\mathrm{Top}}\,T''_{\mathrm{Top}}\right)EQE_{\mathrm{Btm}}\,\phi_{\mathrm{AM1.5G}}\,d\lambda. \quad (9)$$

Note that Eq. (5) includes all losses due to parasitic absorption, and the second summand of Eq. (4) is not included in Eq. (7). Eqs. (7) and (8) allow us to determine the light-generated current of the corresponding cell if the current losses were mitigated, $J_L^0 = J_{SC}^{Exp} + J_{Loss}$. Here we omit the indices $_{\mathrm{Top}}$ and $_{\mathrm{Btm}}$ for better clarity, und use the superscript ^{Exp} (J_{SC}^{Exp}, V_{OC}^{Exp} and η^{Exp}) for the experimentally determined values of the loss-affected device.

We account for the illumination–dependence of the open-circuit voltage using the one-diode model[40]

$$V_{OC}(J_L) = \frac{mk_{\mathrm{B}}T}{q}\ln\left(\frac{J_L}{J_0} + 1\right), \quad (10)$$

with the light-generated current density J_L, the diode ideality factor m, the absolute temperature T, and the Boltzmann constant k_{B}. Throughout this paper the temperature is fixed at 25°C. We model the top cell with an ideality factor of 1 and the bottom cell with an ideality factor of 0.7. J_0 is the diode saturation current density, which is a lumped expression for all recombination pathways, and is calculated from Eq. (9) with the experimental values J_{SC}^{Exp} and V_{OC}^{Exp}. For simplicity we assume the fill factor to not depend on the illumination.

The efficiency of the loss-free cell can then be calculated as

$$\eta^0 = FF^X \cdot J_L^0 \cdot V_{OC}\left(J_L^0\right)/P_{\mathrm{in}}, \quad (11)$$

with P_{in}being the incident light power, and the efficiency loss caused by reflection and parasitic absorption is

$$\eta^0 - \eta^{Exp} = FF^X \cdot \left\{J_L^0 \cdot V_{OC}\left(J_L^0\right) - J_{SC}^{Exp} \cdot V_{OC}^{Exp}\right\}/P_{\mathrm{in}}. \quad (12)$$

Four-terminal module model

Thin-film photovoltaic modules are commonly fabricated by laser patterning of the large-area solar cell layer stack, see Fig. 8. This results in an active area lw for an aperture area $l(w+m)$, with l being the length and w the width of one cell stripe and m the total width lost due to laser scribing. With state-of-the-art techniques, the required three laser scribes result in $m \approx 100\ \mu\mathrm{m}$. Interconnection between individual cells within the module is ensured by the front and back TCOs, each of which cause a relative power loss of [51]

$$\frac{\Delta P}{P} = 2R_{\mathrm{Sh}}\frac{J}{3V}w^2, \quad (13)$$

due to its respective lateral sheet resistance R_{Sh}, with J and V being the current through and the voltage at the TCO. The module efficiency is thus

$$\eta_{\mathrm{Top,Module}} = J_{\mathrm{MPP,Top}}V_{\mathrm{MPP,Top}}\left(1 - 2R_{\mathrm{Sh}}\frac{J_{\mathrm{MPP,Top}}}{3V_{\mathrm{MPP,Top}}}w^2\right)\left(\frac{lw}{l(w+m)}\right)/P_{\mathrm{in}}. \quad (14)$$

$J_{\mathrm{MPP,Top}}$ and $V_{\mathrm{MPP,Top}}$ are the top cell current density and voltage at the maximum power point (MPP), respectively. The factor of 2 comes from the two TCOs. Please note that we neglect shadowing of the top cell by the front TCO, because most TCOs are highly transmittive in the top cell spectral region.

However, the light intensity incident on the bottom cell in the tandem module is reduced by the top cell due to free carrier absorption in the top cell TCOs and the partially intransparent nature of the top cell interconnection. The doping in the top cell TCOs causes absorption by free carriers and thus reduces the light intensity that is incident on the bottom cell. The efficiency of the bottom cell whose short-circuit current is reduced by the weighted absorptance $\langle A\rangle$, and the absorptance of the interconnection areas A_m is

$$\eta_{\mathrm{Btm}} = J_{\mathrm{MPP,Btm}}V_{\mathrm{MPP,Btm}}\left(\left(1 - \langle A_{\mathrm{Top}}\rangle\right)\frac{w}{w+m} + (1 - A_m)\frac{m}{w+m}\right), \quad (15)$$

and the tandem module efficiency

$$\eta_{\mathrm{Total}} = \eta_{\mathrm{Btm}} + \eta_{\mathrm{Top.}} \quad (16)$$

The weighted absorptance $\langle A\rangle$ is the integrated spectral absorptance of the top cell below the top cell absorber band gap λ_{Gap}, weighted with the bottom cell current at each wavelength:

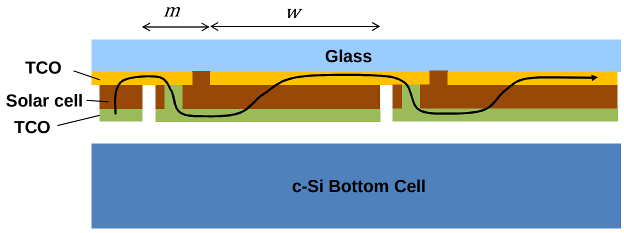

Fig. A1: Interconnection scheme for thin-film minimodules. Three laser scribes are employed to 1. Pattern the front TCO (yellow), 2. Patter the absorber, and 3. Pattern the back TCO to isolate the cells. The photo-active cell width is w, and the width of the photo-inactive interconnection areais m.

$$\langle A \rangle = \int_{\lambda_{\mathrm{Gap}}}^{\infty} A_{Top} EQE_{Btm} \phi_{AM1.5G} d\lambda \Big/ \int_{\lambda_{\mathrm{Gap}}}^{\infty} EQE_{Btm} \phi_{AM1.5G} d\lambda . \quad (17)$$

To calculate $\langle A \rangle$ we assume a top cell band of 800 nm and use the external quantum efficiency EQE_{Btm} of an ideal, 110µm thick c-Si solar cell.[3]

Sample preparation

Silicon heterojunction solar cells were prepared from phosphorous-doped 1 Ωcm, 250 µm thick (100) c-Si wafers as described in.[52]

Perovskite devices were prepared as described in Ref. 10 except for the back contact. PbI_2 was purchased from Sigma-Aldrich and the material CH_3NH_3I was synthesized following the procedure described in Ref. [53]. A compact TiO_2 layer was deposited onto patterned and cleaned FTO (Solaronix, TCO 22-15) substrate by spray pyrolysis at 450 °C using a titanium diisopropoxide bis(acetylacetonate) (75 wt% in 2-propanol, Sigma-Aldrich) diluted in ethanol. A 300 nm thick mesoporous TiO_2 layer was then deposited on the c-TiO_2/FTO substrate by spin coating and annealed to 500 °C. PbI_2 was dissolved in *N*, *N*-dimethylformamide at a concentration of 1M at 70 °C. A PbI_2 solution was then spin coated on m-TiO_2/c-TiO_2/FTO substrate at 6500 r.p.m for 30 s. After drying PbI_2 coated glass at 70 °C for 10 min, the substrate was dipped in a solution of CH_3NH_3I in 2-propanol (10mg ml^{-1}) for 30 s, rinsed with 2-propanol, and dried at 100 °C for 10 min. Spiro-MeOTAD solution was prepared by dissolving 72.3 mg spiro-MeOTAD (Merck), 28.8 µl 4-*tert*-butylpyridine (Sigma-Aldrich), 17.5 µl of a stock solution of 520 mgml^{-1} lithium bis(trifluoromethylsulfonyl)imide (Sigma-Aldrich) in acetonitrile and 14 µl of a stock solution of 300 mg ml^{-1} tris(2-(1H-pyrazol-1-yl)-4-*tert*-butylpyridine)cobalt (III) bis(trifluoromethylsulfonyl)imide (FK209) in acetonitrile, in 1 ml chlorobenzene and spin coated on the perovskite/m-TiO_2/c-TiO_2/FTO substrate at 4000 r.p.m for 30 s. The cells were then finished with either a MoO_x/ITO stack electrode or a MoO_x/Ag electrode. A metal grid was not applied to the perovskite solar cell.

Characterization

Reflection and transmission spectra were recorded with a Perkin Elmer lambda 900 photospectrometer using an integrating sphere. The external quantum efficiency of the top cell was measured in an IMT spectral response setup designed for Si thin-film solar cells, and equipped with a grating monochromator and a xenon lamp. The bottom cell EQE was measured in a commercial PVtools system dedicated for c-Si wafer solar cells. The short-circuit currents were calculated from the EQE measurements. Current-voltage curves were measured in a WACOM sun simulator with 0.25cm^2 and 4 cm^2 shadow masks to define the active cell areas of the top and bottom cell, respectively. For the top cell IV curve, the illumination was set to 0.1 W/cm^2. To measure the IV curve of the bottom cell, the illumination was adjusted with grey filters such that the bottom cell J_{SC} matched the value calculated from the EQE measured in tandem configuration.

Notes and references

[1] École Polytechnique Fédérale de Lausanne (EPFL), Institute of Microengineering (IMT), Photovoltaics and Thin-Film Electronics Laboratory, Rue de la Maladière 71b, 2002 Neuchâtel, Switzerland.

[2] Centre Suisse d'Électronique et de Microtechnique (CSEM), Jaquet-Droz 1, 2002 Neuchâtel, Switzerland.

[3] Laboratory of Nanostructures and Nanomaterials, Institute of Physics, Academy of Sciences of the Czech Republic, v. v. i., Cukrovarnická 10, 162 00 Prague, Czech Republic

1. SEMI, International Technology Roadmap for Photovoltaics (ITRPV), http://www.itrpv.net/Reports/Downloads/2014/, Accessed 30.07.2014.
2. K. Masuko, M. Shigematsu, T. Hashiguchi, D. Fujishima, M. Kai, N. Yoshimura, T. Yamaguchi, Y. Ichihashi, T. Yamanishi, T. Takahama, M. Taguchi, E. Maruyama and S. Okamoto, Achievement of more than 25% conversion efficiency with crystalline silicon heterojunction solar cell, Denver (CO), USA, 2014.
3. A. Richter, M. Hermle and S. W. Glunz, *IEEE J. Photovol.*, 2013, **3**, 1184-1191.
4. D. M. Powell, M. T. Winkler, H. J. Choi, C. B. Simmons, D. B. Needleman and T. Buonassisi, *Energy Environ. Sci.*, 2012, **5**, 5874.
5. P. Gao, M. Grätzel and M. K. Nazeeruddin, *Energy Environ. Sci.*, 2014, **7**, 2448.
6. G. Hodes, *Science*, 2013, **342**, 317-318.
7. A. Kojima, K. Teshima, T. Miyasaka and Y. Shirai, *Meet. Abstr.*, 2006, **MA2006-02**, 397-397.
8. A. Kojima, K. Teshima, Y. Shirai and T. Miyasaka, *Journal of the American Chemical Society*, 2009, **131**, 6050-6051.
9. NREL, NREL Efficiency Chart, http://www.nrel.gov/ncpv/images/efficiency_chart.jpg, Accessed 30.07.2014.
10. J. Burschka, N. Pellet, S.-J. Moon, R. Humphry-Baker, P. Gao, M. K. Nazeeruddin and M. Grätzel, *Nature*, 2013, **499**, 316-319.
11. G. E. Eperon, V. M. Burlakov, P. Docampo, A. Goriely and H. J. Snaith, *Adv. Func. Mater.*, 2014, **24**, 151-157.
12. M. Liu, M. B. Johnston and H. J. Snaith, *Nature*, 2013, **501**, 395-398.
13. P. Docampo, J. M. Ball, M. Darwich, G. E. Eperon and H. J. Snaith, *Nature communications*, 2013, **4**, 2761.
14. J. You, Z. Hong, Y. Yang, Q. Chen, M. Cai, T.-B. Song, C.-C. Chen, S. Lu, Y. Liu, H. Zhou and Y. Yang, *ACS Nano*, 2014, **8**, 1674-1680.
15. J. M. Ball, M. M. Lee, A. Hey and H. J. Snaith, *Energy Environ. Sci.*, 2013, **6**, 1739-1743.
16. K. Wojciechowski, M. Saliba, T. Leijtens, A. Abate and H. J. Snaith, *Energy Environ. Sci.*, 2014, **7**, 1142-1147.
17. H.-S. Kim, C.-R. Lee, J.-H. Im, K.-B. Lee, T. Moehl, A. Marchioro, S.-J. Moon, R. Humphry-Baker, J.-H. Yum, J. E. Moser, M. Grätzel and N.-G. Park, *Sci. Rep.*, 2012, **2**.
18. G. E. Eperon, S. D. Stranks, C. Menelaou, M. B. Johnston, L. M. Herz and H. J. Snaith, *Energy Environ. Sci.*, 2014, **7**, 982-988.

19. S. De Wolf, J. Holovsky, S.-J. Moon, P. Löper, B. Niesen, M. Ledinsky, F.-J. Haug, J.-H. Yum and C. Ballif, *J. Phys. Chem. Lett.*, 2014, **5**, 1035-1039.
20. H. J. Snaith, *J. Phys. Chem. Lett.*, 2013, **4**, 3623-3630.
21. M. A. Green, A. Ho-Baillie and H. J. Snaith, *Nat Photon*, 2014, **8**, 506-514.
22. R. F. Service, *Science*, 2013, **342**, 794-797.
23. R. F. Service, *Science*, 2014, **344**, 458-458.
24. M. McGehee, Optimizing Perovskite Semiconductors for Tandem Solar Cells, MRS Spring Meeting, San Francisco, CA, USA, 2014.
25. P. Löper, B. Niesen, S. Moon, S. Martin de Nicolas, J. Holovsky, Z. Remes, M. Ledinsky, F. Haug, J. Yum, S. De Wolf and C. Ballif, *IEEE J. Photovol.*, 2014, **4**, 1545-1551.
26. G. E. Eperon, V. M. Burlakov, A. Goriely and H. J. Snaith, *ACS Nano*, 2014, **8**, 591-598, supporting information.
27. C. Roldán-Carmona, O. Malinkiewicz, A. Soriano, G. Mínguez Espallargas, A. Garcia, P. Reinecke, T. Kroyer, M. I. Dar, M. K. Nazeeruddin and H. J. Bolink, *Energy Environ. Sci.*, 2014, **7**, 994.
28. Z. M. Beiley, M. G. Christoforo, P. Gratia, A. R. Bowring, P. Eberspacher, G. Y. Margulis, C. Cabanetos, P. M. Beaujuge, A. Salleo and M. D. McGehee, *Adv Mater*, 2013, **25**, 7020-7026.
29. G. Y. Margulis, M. G. Christoforo, D. Lam, Z. M. Beiley, A. R. Bowring, C. D. Bailie, A. Salleo and M. D. McGehee, *Advanced Energy Materials*, 2013, **3**, 1657-1663.
30. J. Gjessing, E. S. Marstein and A. Sudbø, *Opt. Express*, 2010, **18**, 5481-5495.
31. B. Demaurex, S. De Wolf, A. Descoeudres, Z. Charles Holman and C. Ballif, *Appl. Phys. Lett.*, 2012, **101**, 171604.
32. C. Battaglia, S. Martín de Nicolás, S. De Wolf, X. Yin, M. Zheng, C. Ballif and A. Javey, *Appl. Phys. Lett.*, 2014, **104**.
33. Y. Zhao, A. M. Nardes and K. Zhu, *Appl. Phys. Lett.*, 2014, **104**, 213906.
34. D. Pysch, A. Mette and S. W. Glunz, *Sol. Energ. Mat. Sol. Cells*, 2007, **91**, 1698-1706.
35. Z. C. Holman, A. Descoeudres, S. De Wolf and C. Ballif, *IEEE J. Photovol.*, 2013, **3**, 1243-1249.
36. S. De Wolf, A. Descoeudres, Z. C. Holman and C. Ballif, *Green*, 2012, **2**, 7-24.
37. R. A. Smith, *Semiconductors*, Cambridge University Press, New York, USA, 1978.
38. U. Bach, D. Lupo, P. Comte, J. E. Moser, F. Weissörtel, J. Salbeck, H. Spreitzer and M. Grätzel, *Nature*, 1998, **395**, 583-585.
39. J. Burschka, A. Dualeh, F. Kessler, E. Baranoff, N.-L. Cevey-Ha, C. Yi, M. K. Nazeeruddin and M. Grätzel, *Journal of the American Chemical Society*, 2011, **133**, 18042-18045.
40. P. Würfel, *Physics of Solar Cells - From principles to new concepts*, Wiley-Vch Verlag GmbH & Co KgaA, Weinheim, 2005.
41. M. Taguchi, A. Yano, S. Tohoda, K. Matsuyama, Y. Nakamura, T. Nishiwaki, K. Fujita and E. Maruyama, *IEEE J. Photovol.*, 2014, **4**, 96-99.
42. L. Barraud, Z. C. Holman, N. Badel, P. Reiss, A. Descoeudres, C. Battaglia, S. De Wolf and C. Ballif, *Sol. Energ. Mat. Sol. Cells*, 2013, **115**, 151-156.
43. L. Ding, S. Nicolay, J. Steinhauser, U. Kroll and C. Ballif, *Adv. Func. Mater.*, 2013, **23**, 5177-5182.
44. H. Zhou, Q. Chen, G. Li, S. Luo, T.-b. Song, H.-S. Duan, Z. Hong, J. You, Y. Liu and Y. Yang, *Science*, 2014, **345**, 542-546.
45. F. Matteocci, S. Razza, F. Di Giacomo, S. Casaluci, G. Mincuzzi, T. M. Brown, A. D'Epifanio, S. Licoccia and A. Di Carlo, *Physical chemistry chemical physics : PCCP*, 2014, **16**, 3918-3923.
46. J. Liu, Y. Wu, C. Qin, X. Yang, T. Yasuda, A. Islam, K. Zhang, W. Peng, W. Chen and L. Han, *Energy Environ. Sci.*, 2014.
47. A. Kanevce and W. K. Metzger, *J. Appl. Phys.*, 2009, **105**.
48. J. H. Noh, S. H. Im, J. H. Heo, T. N. Mandal and S. I. Seok, *Nano Lett.*, 2013, **13**, 1764-1769.
49. S. A. Kulkarni, T. Baikie, P. P. Boix, N. Yantara, N. Mathews and S. Mhaisalkar, *J. Mater. Chem. A*, 2014, **2**, 9221.
50. IEC, *Photovoltaic devices - part 3: measurement principles for terrestrial photovoltaic (PV) solar devices with reference spectral irradiance data*, International Electrotechnical Commission, 2008.
51. A. Shah, *Thin-Film Silicon Solar Cells*, EPFL Press, 2010.
52. A. Descoeudres, Z. C. Holman, L. Barraud, S. Morel, S. De Wolf and C. Ballif, *IEEE J. Photovol.*, 2013, **3**, 83-89.
53. J.-H. Im, J. Chung, S.-J. Kim and N.-G. Park, *Nanoscale Research Letters*, 2012, **7**.